remote sensing

MDPI

Article

An Efficient Spectrum Reconstruction Algorithm for Non-Uniformly Sampled Signals and Its Application in Terahertz SAR

Guohua Zhang [1], Chao Li [2,*], Zeyu Wang [1], Jianmin Hu [2], Shen Zheng [2], Xiaojun Liu [2] and Guangyou Fang [2]

[1] Aerospace Information Research Institute, Chinese Academy of Sciences, Beijing 100094, China; zhangguohua21@mails.ucas.ac.cn (G.Z.); wangzeyu20@mails.ucas.ac.cn (Z.W.)
[2] The Key Laboratory of Electromagnetic Radiation and Sensing Technology, Chinese Academy of Sciences, Beijing 100190, China; hujm@aircas.ac.cn (J.H.); zhengshen@aircas.ac.cn (S.Z.); lxjdr@mail.ie.ac.cn (X.L.); gyfang@mail.ie.ac.cn (G.F.)
* Correspondence: cli@mail.ie.ac.cn

Abstract: An efficient spectrum reconstruction algorithm based on the Tikhonov regularization for terahertz (THz) synthetic aperture radar (SAR) azimuth non-uniform sampling is proposed in this article. The high bandwidth, high azimuth resolution, and high frame rate characteristics of THz SAR contribute to its wide application prospects in both military and civilian remote sensing fields. However, the higher azimuth sampling rate also leads to the more severe non-uniform sampling issues of THz SAR. Traditional methods based on the hardware adjustment of pulse repetition frequency (PRF) and simple interpolation for azimuth resampling struggle to meet the higher imaging quality requirements. The back projection algorithm (BPA) can accurately focus non-uniformly sampled data but requires significant computational resources. The algorithm proposed in this paper, which can reconstruct the wavenumber spectrum of SAR azimuth non-uniformly sampled signals, transforms the spectrum reconstruction problem into a linear equation system and solves it using Tikhonov regularization, thereby exhibiting higher computational efficiency compared to BPA. Furthermore, the proposed algorithm is derived from precise theoretical formulations and controls the solution error by utilizing a regularization parameter, leading to a superior imaging quality compared to the azimuth resampling algorithm. In this paper, an accurate spectrum reconstruction formula of non-uniform sampling signals with a finite length is derived, the influence of noise error on the solution is analyzed, and the THz SAR azimuth non-uniform sampling signals are processed from the wavenumber domain. Finally, simulation and experimental results verify the effectiveness of the proposed algorithm.

Keywords: azimuth non-uniform sampling; spectrum reconstruction; Tikhonov regularization; terahertz (THz) synthetic aperture radar (SAR)

check for updates

Citation: Zhang, G.; Li, C.; Wang, Z.; Hu, J.; Zheng, S.; Liu, X.; Fang, G. An Efficient Spectrum Reconstruction Algorithm for Non-Uniformly Sampled Signals and Its Application in Terahertz SAR. *Remote Sens.* **2023**, *15*, 4427. https://doi.org/10.3390/rs15184427

Academic Editor: Dusan Gleich

Received: 27 August 2023
Accepted: 1 September 2023
Published: 8 September 2023

Copyright: © 2023 by the authors. Licensee MDPI, Basel, Switzerland. This article is an open access article distributed under the terms and conditions of the Creative Commons Attribution (CC BY) license (https://creativecommons.org/licenses/by/4.0/).

1. Introduction

Synthetic aperture radar has been widely applied in various fields such as ocean observation, cartography, and civilian remote sensing due to its imaging characteristics and all-day, all-weather, and high azimuth resolutions [1,2]. Compared to microwave SAR, THz SAR offers a shorter wavelength, wider bandwidth, and distinct Doppler characteristics resulting from platform or target motion. This enables THz SAR to achieve a higher imaging resolution [3] and real-time detection capabilities at video frame rates [4], thus presenting broader application prospects.

The integrated navigation system based on the Global Navigation Satellite System (GNSS) and Inertial Navigation System (INS) allows for real-time acquisition of the position and attitude information of radar platforms, finding effective application in synthetic aperture radar systems [5]. For vehicle-borne or airborne SAR systems, although an

integrated navigation system can periodically record the position information of the radar, the non-uniform sampling characteristics in azimuth are inevitable due to the difficulty in maintaining an ideal constant linear motion during radar movement [6], which leads to a degradation in the imaging quality of the radar. Compared to microwave SAR, THz SAR requires a higher sampling rate in azimuth, resulting in more severe non-uniform sampling issues that significantly impact the image reconstruction.

Traditional methods for addressing non-uniform sampling in the azimuth of microwave SAR primarily focus on hardware considerations. By utilizing an integrated navigation system to measure the real-time motion velocity of the radar platform, the PRF can be adjusted to achieve a more uniform azimuth sampling position [7]. However, for THz SAR systems with denser sampling points in azimuth, this hardware-based method of adjusting the PRF has certain limitations. The azimuth sampling positions still remain somewhat non-uniform to some extent, making it difficult to achieve the desired imaging results. In addition, a higher azimuth sampling rate also increases the hardware design requirements and incurs additional hardware costs.

The issue of non-uniform sampling in the azimuth of SAR can also be addressed from a software perspective. The flight path error of the SAR platform can be divided into along-track motion errors and cross-track motion errors [8]. The along-track motion error is the azimuth non-uniform sampling problem studied in this paper. On the other hand, the cross-track motion error, caused by the deviation of the radar platform from the ideal motion trajectory, is typically compensated for after compensating for the along-track motion error. Based on the importance of the impact on imaging quality, there is a considerable amount of literature that has studied the problem of cross-track motion error compensation [5–15], while research on the problem of along-track motion error compensation is relatively limited, even though its impact on imaging quality should not be overlooked [16]. Currently, the predominant approach for addressing the issue is azimuth resampling [10], which involves interpolating the non-uniformly sampled data to obtain uniformly sampled echo data for processing. This method is straightforward in principle; however, when the influence of spectral aliasing cannot be neglected, it results in a degradation of the image focusing effect [17]. The BPA, being a time-domain imaging technique, is applicable to any imaging geometry and can also be used for imaging non-uniformly sampled echo data [8]. This method offers high imaging accuracy but requires significant computational resources. A phase compensation-based method was employed in [17] to compensate for along-track motion errors, which offers high computational efficiency. However, this method relies on certain approximations and lacks general applicability, particularly for imaging scenarios involving close-range distances. Due to the distance having no influence on the spectral range of azimuth signals, the spectral reconstruction method can effectively handle imaging issues in close-range scenarios. The problem of spectral reconstruction for azimuth non-uniformly sampled signals can be formulated as an inverse problem in mathematics, and the solution to this problem may be ill-posed. Therefore, we employ the Tikhonov regularization method for solving the problem of spectral reconstruction. The Tikhonov regularization method is an approach that, overall, minimizes the norm of the solution and residual norm based on the selected regularization parameter [18]. It has been widely applied in solving ill-posed problems [19,20].

To tackle the problem of non-uniform sampling in the azimuth of THz SAR, a regularization-based algorithm in this paper is proposed for reconstructing the spectrum of non-uniformly sampled signals. It transforms the spectrum reconstruction problem into a linear equation system and solves it using Tikhonov regularization. The proposed algorithm achieves a fast transformation of SAR non-uniformly sampled signals from the spatial domain to wavenumber domain in azimuth, thereby establishing an efficient image reconstruction algorithm suitable for non-uniformly sampled SAR. Considering the characteristics of SAR echo signals as two-dimensional matrices and unknown noise, a regularization parameter selection method based on L-curve criterion is established. Moreover, we utilize a Fourier series to analyze the error in spectrum reconstruction, demonstrating

that the accuracy of estimating the signal spectrum for finite-length approximate band-limited signals depends on the high-frequency components beyond the signal bandwidth and the signal noise. The simulation and experimental results validate that the proposed algorithm achieves a more accurate reconstruction of the non-uniformly sampled signals compared to the azimuth resampling algorithms, resulting in improved imaging quality. Additionally, it offers higher computational efficiency compared to BPA, making it more suitable for compensating the significant azimuth motion errors in THz SAR applications.

This article is organized as follows. In Section 2, a spectral reconstruction model for non-uniformly sampled signals is established. In Section 3, the Tikhonov regularization method is used to solve the model and the regularization parameter is determined using the L-curve criterion. In Section 4, the proposed method is applied to the problem of THz SAR with non-uniform sampling, and a corresponding algorithm flowchart is provided. In Section 5, simulations and experiments are conducted using a 0.3 THz stepped-frequency radar system. Finally, a conclusion is drawn in Section 6.

2. Spectrum Reconstruction Model for Non-Uniform Sampling Signals

For a finite-length continuous signal $s_l(t)$, where $t \in [0, T_l)$, let $\Delta f_l = 1/T_l$, assuming it satisfies the Dirichlet condition and its spectrum is primarily concentrated within the frequency range of $[-M\Delta f_l, M\Delta f_l]$; with high-frequency components being negligible, we define a signal meeting these conditions as an approximate band-limited signal, which is commonly observed in most real-world sampled analog signals.

Let $S_l(f)$ be the Fourier transform of $s_l(t)$. Given N non-uniform sampling positions with known sampling values $s(i) = s_l(t_i)$, where $0 \leq t_1 < t_2 \cdots < t_N < T_l$, and s is an N-dimensional vector, the frequency spectrum of $s_l(t)$ to be reconstructed is denoted as a $(2M+1)$-dimensional vector S, with the condition that

$$S(m) = S_l[(m-1-M)\Delta f_l] \quad m = 1, 2, \cdots 2M+1. \tag{1}$$

Define A as a linear operator, represented by an $N \times (2M+1)$-dimensional matrix, satisfying the condition

$$s = AS + \tilde{n} \tag{2}$$

where $\tilde{n}$ is the error term caused by $s_l(t)$ not being a true band-limited signal.

Equation (2) represents the spectrum reconstruction model for non-uniformly sampled signals, which allows us to estimate the discrete signal spectrum S given the known vector s and matrix A. Next, we will derive the expressions for A and $\tilde{n}$, and analyze the magnitude of $\tilde{n}$ through simulations.

2.1. Principle of Spectrum Reconstruction

For an infinite-length periodic signal $s_c(t)$ with a frequency band of $[-M\Delta f_c, M\Delta f_c]$ and a signal period of $T_c = 1/\Delta f_c$, the value of any point t in $s_c(t)$ can be accurately expressed using the following discrete inverse Fourier transform formula [21]:

$$s_c(t) = \sum_{k=-M}^{M} \hat{s}_c(k) e^{j2\pi k \Delta f_c t} \tag{3}$$

where $\hat{s}_c(k)$ is the Fourier coefficient of $s_c(t)$ at frequency $f = k\Delta f_c$.

However, for finite-length signals typically encountered in the real-world, they do not satisfy (3). Nevertheless, it is worth noting that (3) approximately holds for an approximate band-limited signal, with the error value depending on the spectral components outside the signal's bandwidth.

Let $\tilde{s}_l(t)$ be the periodic extension of $s_l(t)$, satisfying $\tilde{s}_l(t + nT_l) = s_l(t)$, where $t \in [0, T_l)$, and n is an integer. Then, $\tilde{s}_l(t)$ can be expanded using the Fourier series [22], given by

$$\tilde{s}_l(t) = \sum_{n=-\infty}^{\infty} C_n e^{j2\pi n \frac{t}{T_l}} \tag{4}$$

where C_n is the Fourier coefficient of $\tilde{s}_l(t)$, and the expression is

$$C_n = \frac{1}{T_l}\int_0^{T_l} \tilde{s}_l(t) e^{-j2\pi n \frac{t}{T_l}} dt = \frac{1}{T_l}\int_0^{T_l} s_l(t) e^{-j2\pi n \Delta f_l t} dt = \frac{1}{T_l} S_l(n\Delta f_l). \tag{5}$$

This indicates that C_n is equal to the value of $S_l(f)$ at $f = n\Delta f_l$ multiplied by a constant term. When $t \in [0, T_l)$, it holds that

$$\begin{aligned} s_l(t) = \tilde{s}_l(t) &= \sum_{n=-\infty}^{\infty} C_n e^{j2\pi n \frac{t}{T_l}} = \sum_{n=-\infty}^{\infty} C_n e^{j2\pi n \Delta f_l t} \\ &= \sum_{n=-M}^{M} C_n e^{j2\pi n \Delta f_l t} + \sum_{n=-\infty}^{-M+1} C_n e^{j2\pi n \Delta f_l t} + \sum_{n=M+1}^{\infty} C_n e^{j2\pi n \Delta f_l t} \end{aligned} \tag{6}$$

Let

$$\delta_l^M(t) = \sum_{n=-\infty}^{-M+1} C_n e^{j2\pi n \Delta f_l t} + \sum_{n=M+1}^{\infty} C_n e^{j2\pi n \Delta f_l t} \tag{7}$$

then (6) can be rewritten as

$$s_l(t) = \sum_{n=-M}^{M} C_n e^{j2\pi n \Delta f_l t} + \delta_l^M(t), \quad t \in [0, T_l). \tag{8}$$

As the spectrum of $s_l(t)$ is primarily concentrated within the range $[-M\Delta f_l, M\Delta f_l]$, it suggests that when $|n| > M$, the magnitude of C_n is close to zero. Therefore, $\delta_l^M(t)$ is significantly smaller compared to the first term on the right side of (8). For N non-uniform sampling positions t_i, let vector $\delta^M(i) = \delta_l^M(t_i)$, then, the norm of δ^M is much smaller than the norm of s, i.e., $\left\|\delta^M\right\| \ll \|s\|$. We define δ^M as the higher-order error term of the non-uniform sampling signal. From a time-domain perspective, δ^M can be expressed as the error generated by approximating a finite-length signal using a certain order of trigonometric polynomials. As the order increases, the approximation error decreases.

Based on (2), (5), and (8), the error term can be obtained as $\tilde{n} = \delta^M$, and the expression for A is

$$A = \frac{1}{T_l}\begin{bmatrix} \exp(-j2\pi M\Delta f_l \mathrm{t}_1) & \exp(-j2\pi(M-1)\Delta f_l \mathrm{t}_1) & \cdots & \exp(j2\pi M\Delta f_l t_1) \\ \exp(-j2\pi M\Delta f_l t_2) & \exp(-j2\pi(M-1)\Delta f_l t_2) & \cdots & \exp(j2\pi M\Delta f_l t_2) \\ \vdots & \vdots & \cdots & \vdots \\ \exp(-j2\pi M\Delta f_l t_N) & \exp(-j2\pi(M-1)\Delta f_l t_N) & \cdots & \exp(j2\pi M\Delta f_l t_N) \end{bmatrix} \tag{9}$$

2.2. Simulation Analysis of High-Order Error Term δ^M

The selected simulation signals are $s_1(t) = \sin(2000\pi t), 0 \le t < 0.1$ for the sine wave signal and $s_2(t) = \cos[2000\pi(t - 0.05)^2], 0 \le t < 0.1$ for the linear frequency modulation (LFM) signal. The time-domain waveform plots of the non-uniformly sampled signals $s_1(t)$ and $s_2(t)$, represented as $s_1(t_i^{(1)})$ and $s_2(t_i^{(2)})$, respectively, are shown in Figure 1a,b, where $i = 1, 2, \cdots, N$. The non-uniform sampling points $t_i^{(1)}$ and $t_i^{(2)}$ are randomly obtained within the range of $[0, 0.1)$. The frequency spectra of $s_1(t)$ and $s_2(t)$ are primarily centered at the interval of $[-1000, 1000]$. To improve the accuracy of the computations, the actual spectral bandwidth used for the calculations should be slightly wider than the theoretical spectral bandwidth of the signal [23]. We set the oversampling factor $a = 1.2$, which means that the actual computational spectral range of both signals is set to $[-1200, 1200]$.

Consequently, we have $M = 1200/\Delta f = 120$, and choose the number of non-uniform sampling points for the two signals as $N = \lfloor 1.2 \times (2M+1) \rfloor = 289$.

Since $\tilde{n} = \delta^M$, we can solve it using (2). Let S_1 and S_2 be the discrete frequency spectrum vectors of $s_1(t)$ and $s_2(t)$, and they have the same meaning as the variable S in Equation (2). The values of S_1 and S_2 are obtained by performing the fast Fourier transform (FFT) operation on the uniformly sampled signals of $s_1(t)$ and $s_2(t)$, which are sampled at a rate ten times higher than the Nyquist sampling rate [24]. The A is generated based on the positions of the non-uniform sampling points. The waveform comparison between the non-uniformly sampled signals and obtained by multiplying A with the discrete frequency spectrum vectors are shown in Figure 1c,d. By subtracting the amplitudes of the two waveforms being compared, we can obtain δ^M of the two non-uniformly sampled signals, which are shown in Figure 1e,f, respectively. The simulation results indicate that compared to $s_1(t_i^{(1)})$ and $s_2(t_i^{(2)})$, δ^M is significantly smaller. The ratio of $\|\delta^M\|/\|s\|$ in $s_1(t_i^{(1)})$ and $s_2(t_i^{(2)})$ is found to be 5.176×10^{-14} and 0.003, respectively, satisfying the condition of $\|\delta^M\| \ll \|s\|$. This also demonstrates that estimating the discrete frequency spectrum of non-uniformly sampled signals using (2) is feasible, as δ^M is significantly smaller compared to s.

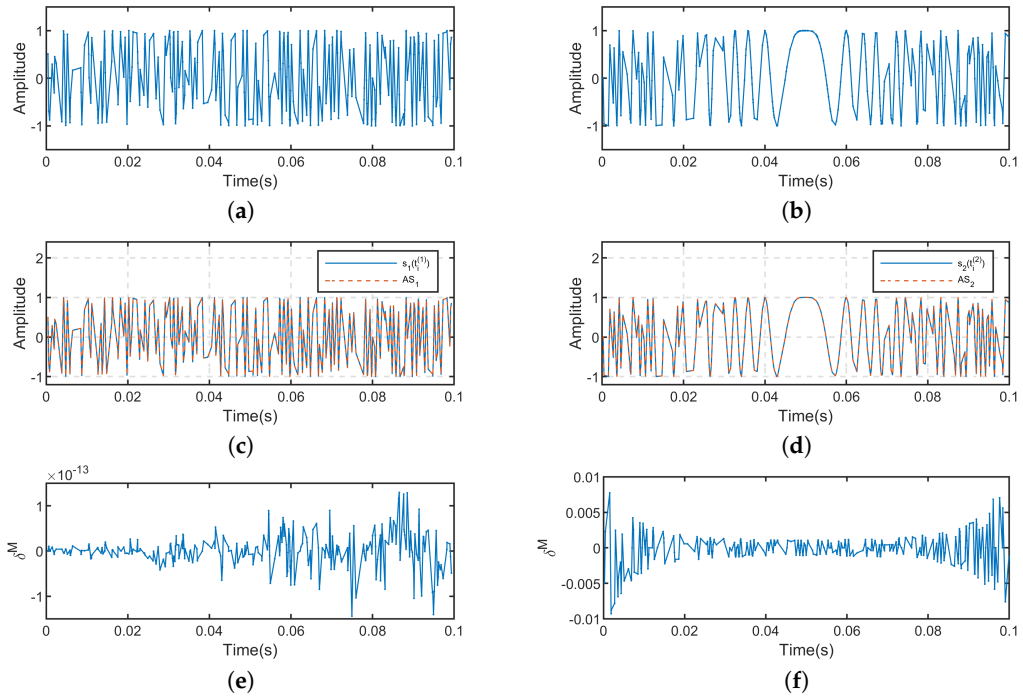


Figure 1. (**a**) Time-domain waveform of $s_1(t_i^{(1)})$. (**b**) Time-domain waveform of $s_2(t_i^{(2)})$. (**c**) Waveform comparison between $s_1(t_i^{(1)})$ and AS_1. (**d**) Waveform comparison between $s_2(t_i^{(2)})$ and AS_2. (**e**) The high-order error term δ^M of $s_1(t_i^{(1)})$. (**f**) The high-order error term δ^M of $s_2(t_i^{(2)})$.

3. Model Solution

The sampled signals are inevitably contaminated with noise. Assume the actual non-uniformly sampled signal is represented by the vector s_δ, where $s_\delta = s + \delta$, δ indicating the noise error term. In this case, the error term $\tilde{n}$ should also include the effects caused by the noise, let $\tilde{n} = \delta^M + \delta$. Therefore, according to (2), we can get

$$s_\delta = AS + \tilde{n} \tag{10}$$

Equation (10) represents the signal model that needs to be solved under the presence of noise. By setting $AS_{\tilde{n}} = AS + \tilde{n}$ and $S_{\tilde{n}}$ as the approximate solution of S, Equation (10) can be equivalently expressed as

$$s_\delta = AS_{\tilde{n}} \tag{11}$$

In this article, we only consider the case when $N \geq 2M+1$, indicating that the signal's sampling rate is not less than the Nyquist sampling rate, and Equation (11) has a unique least squares solution.

3.1. Tikhonov Regularization and Solution Error Analysis

The singular value decomposition (SVD) of A is

$$A = U\Sigma V^* \tag{12}$$

where V is an orthogonal matrix composed of the corresponding eigenvectors $(v_1, \cdots, v_{2M+1})$ of A^*A with eigenvalues $\lambda_1 \geq \lambda_2 \geq \cdots \geq \lambda_{2M+1} > 0$, and all eigenvalues of A^*A are positive real numbers. Σ is the singular value matrix, satisfying $\Sigma(i,i) = \sigma_i, i \leq 2M+1$, where $\sigma(i) = \sqrt{\lambda_i}$ is the singular values of A. U is an orthogonal matrix of dimension $N \times N$, and its columns are formed by the vectors$(u_1, \cdots, u_N)$.

Suppose $S^0_{\tilde{n}}$ is the least squares solution of (2). Based on Picard's theorem [25], it can be expressed as

$$S^0_{\tilde{n}} = A^+ s_\delta = \sum_{j=1}^{2M+1} \frac{\langle s_\delta, u_j \rangle}{\sigma_j} v_j \tag{13}$$

When there are certain singular values σ_j of A that are very small or close to zero, the solution for Equation (11) becomes ill-posed. In this case, $\tilde{n}$ has a significant impact on the solution. To solve such problems, a Tikhonov regularization operator $R_\alpha : C^N \to C^{2M+1}$ is constructed [26], such that

$$S^\alpha_{\tilde{n}} = R_\alpha s_\delta = \sum_{j=1}^{2M+1} \frac{q(\alpha,\sigma_j)}{\sigma_j} \langle s_\delta, u_j \rangle v_j \quad \alpha > 0 \tag{14}$$

where $S^\alpha_{\tilde{n}}$ is the regularized solution of Equation (13) under the regularization parameter α, and $q(\alpha, \sigma_j)$ is the filtering factor [27]. For small singular values σ_j, $q(\alpha, \sigma_j)$ can attenuate the amplification effect of $1/\sigma_j^2$ on the error, thereby obtaining a stable solution for Equation (13). The expression for the filtering factor is

$$q(\alpha, \sigma_j) = \frac{\sigma_j^2}{\alpha^2 + \sigma_j^2} \quad \alpha > 0, 0 \leq \sigma_j \leq \|A\| \tag{15}$$

Let

$$z = \sqrt{\sum_{j=1}^{2M+1} \frac{1}{\sigma_j^2} \left| \langle S, v_j \rangle \right|^2} \tag{16}$$

utilizing the Tikhonov regularization method to quantify the solution error of Equation (10) as

$$\left\| S^\alpha_{\tilde{n}} - S \right\| \leq \frac{1}{2\alpha} \|\tilde{n}\| + \frac{\alpha}{2} z \tag{17}$$

The specific formula derivation can be found in Appendix A. The result of Equation (17) indicates that, when a non-uniform sampling problem is determined, the solving error is only dependent on α, as the magnitude of $\|\tilde{n}\|$ and z can be considered as unknown constants. The solving error caused by $\tilde{n}$ decreases as α increases. When $\alpha \to \infty$, this term tends to zero. The second term on the right-hand side of Equation (17) represents the regularization error caused by filter factor and increases with the increase of α

The magnitude of solving error for $s_2(t_i^{(2)})$ under different α is shown in Figure 2. The 500 selected regularization parameters are evenly distributed on a logarithmic scale

axis lg α with the range of $[\sigma_1, \sigma_{2M+1}]$. When α is small, the solving error primarily caused by $\tilde{n}$ reaches the order of 10^5, indicating that $\tilde{n}$ has a significant impact on the solution results for $s_2(t_i^{(2)})$. As α increases, the solving error gradually decreases, reaching its minimum value when $\alpha = 5.885 \times 10^{-7}$. However, as α further increases, the regularization error begins to dominate. Therefore, the role of α is to balance the two types of errors in Equation (17). In practical solutions to non-uniform sampling problems, it is important to select an appropriate α in order to minimize the overall solving error as much as possible.

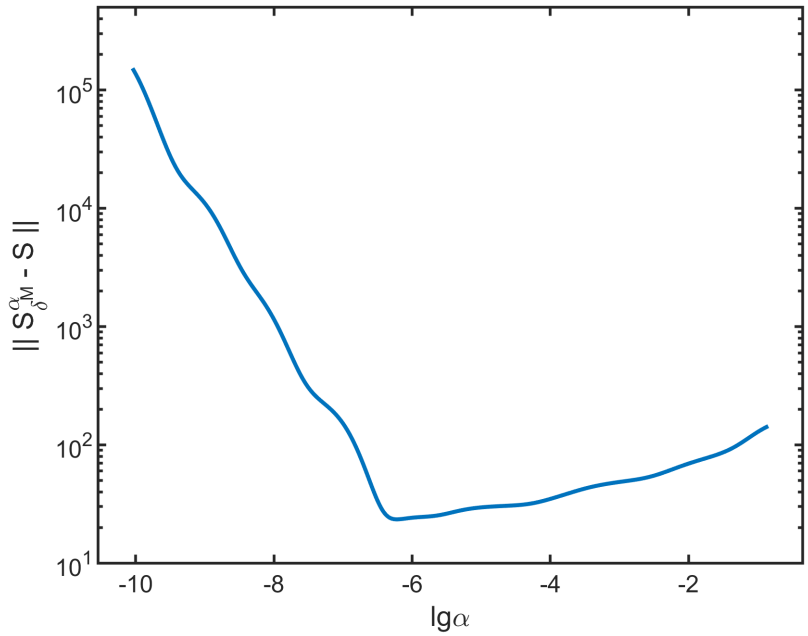


Figure 2. The solving error of Tikhonov regularization for $s_2(t_i^{(2)})$ under different α.

3.2. Selection of Regularization Parameters and Simulation

Considering that it is difficult to obtain prior knowledge about $\tilde{n}$ in practical non-uniform sampling problems, we adopt the L-curve criterion to select α. The L-curve is used to describe the relationship between the residual term $\left\| AS_{\tilde{n}}^{\alpha} - s_\delta \right\|$ and the regularized solution $\left\| S_{\tilde{n}}^{\alpha} \right\|$ under different α. it can effectively utilize the information of $\left\| AS_{\tilde{n}}^{\alpha} - s_\delta \right\|$ and $\left\| S_{\tilde{n}}^{\alpha} \right\|$, seeking a balance that ensures both values are relatively small [28]. In order to avoid an excessively large regularized solution, we impose a constraint on the norm of $S_{\tilde{n}}^{\alpha}$ within a certain range. In this case, we select the corner point of the L-curve, which corresponds to the regularization parameter value that maximizes the curvature of the L-curve on a log–log scale. Let $\rho = \log\left\| AS_{\tilde{n}}^{\alpha} - s_\delta \right\|$ and $\vartheta = \log\left\| S_{\tilde{n}}^{\alpha} \right\|$, then the chosen α is determined to maximize the following curvature function $c(\alpha)$ within a specified range [29].

$$c(\alpha) = \frac{\rho' \vartheta'' - \rho'' \vartheta'}{\left((\rho')^2 + (\vartheta')^2\right)^{\frac{3}{2}}} \tag{18}$$

where $'$ represents the derivative with respect to α. Given the known singular value decomposition of A, it is straightforward to numerically solve for the regularization parameter that maximizes the curvature function $c(\alpha)$.

The solving results of $s_1(t_i^{(1)})$ and $s_2(t_i^{(2)})$ using the Tikhonov regularization method based on L-curve criterion are shown in Figure 3. In Figure 3a,c, the numbers marked with 'x' represent the values of regularization parameter at those points. The positions marked by the red dashed lines on L-curve indicate the points with maximum curvature. The selected regularization parameters are 3.5933×10^{-12} for $s_1(t_i^{(1)})$ and 5.3568×10^{-7} for $s_2(t_i^{(2)})$. It can be observed from Section 3.1 that the regularization parameter selected for $s_2(t_i^{(2)})$

based on L-curve criterion is in the same order of magnitude as the one which minimizes the difference from true solution, and there is a very small error present. Compared to $s_1(t_i^{(1)})$, $s_2(t_i^{(2)})$ is more affected by errors. Therefore, the L-curve exhibits a noticeable corner in Figure 3c and the spectrum of $s_1(t_i^{(1)})$ can be perfectly reconstructed in Figure 3b. Moreover, by comparing the results in Figure 3d, we can find that even under conditions where the influence of errors is significant, the proposed algorithm is still able to achieve satisfactory spectral reconstruction results.

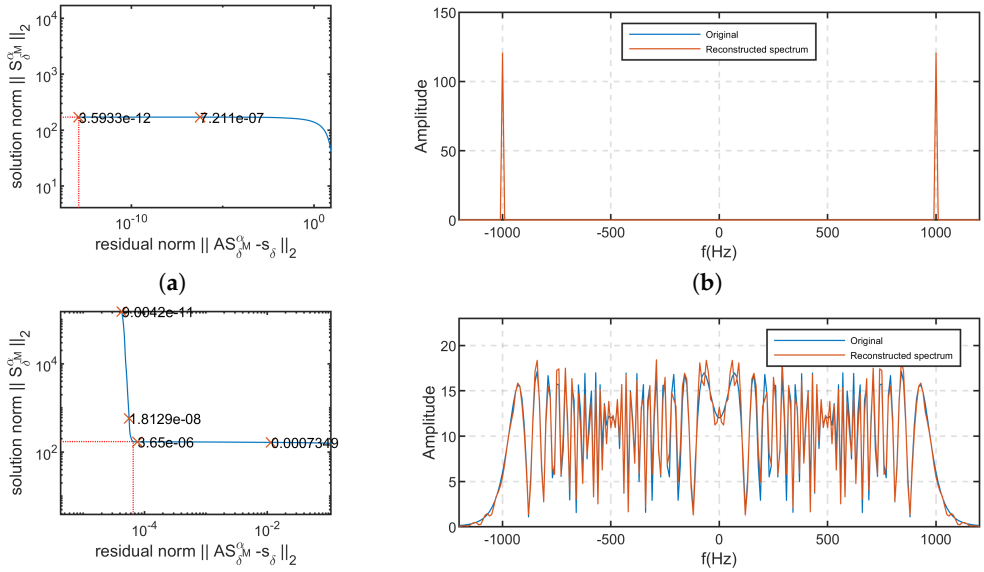


Figure 3. (**a**) L-curve for $s_1(t_i^{(1)})$. (**b**) The results of Tikhonov regularization for the spectrum reconstruction of $s_1(t_i^{(1)})$. (**c**) L-curve for $s_2(t_i^{(2)})$. (**d**) The results of Tikhonov regularization for the spectrum reconstruction of $s_2(t_i^{(2)})$.

To further verify the effectiveness of the proposed algorithm, we transform the reconstructed signal's spectrum to the time domain using discrete inverse Fourier transform and compare it with the results obtained through cubic spline interpolation. The cubic spline interpolation method is commonly used due to its simplicity and excellent stability, and it is also frequently employed in addressing the azimuth non-uniform sampling problem in SAR. Therefore, we compare the proposed method with the cubic spline interpolation. Figure 4a–d shows the results of reconstructing $s_1(t_i^{(1)})$ and $s_2(t_i^{(2)})$ using both methods and comparing them with the original uniformly sampled signals. Figure 4e,f illustrates the comparison results of solving errors between the two methods. This indicate that the proposed method significantly outperforms cubic spline interpolation in terms of reconstructing signals $s_1(t_i^{(1)})$ and $s_2(t_i^{(2)})$. Particularly for $s_1(t_i^{(1)})$, the reconstruction result obtained through cubic spline interpolation is very poor due to spectral aliasing effect, while the proposed method can get accurately reconstruction results, with solution errors in the order of 10^{-10}.

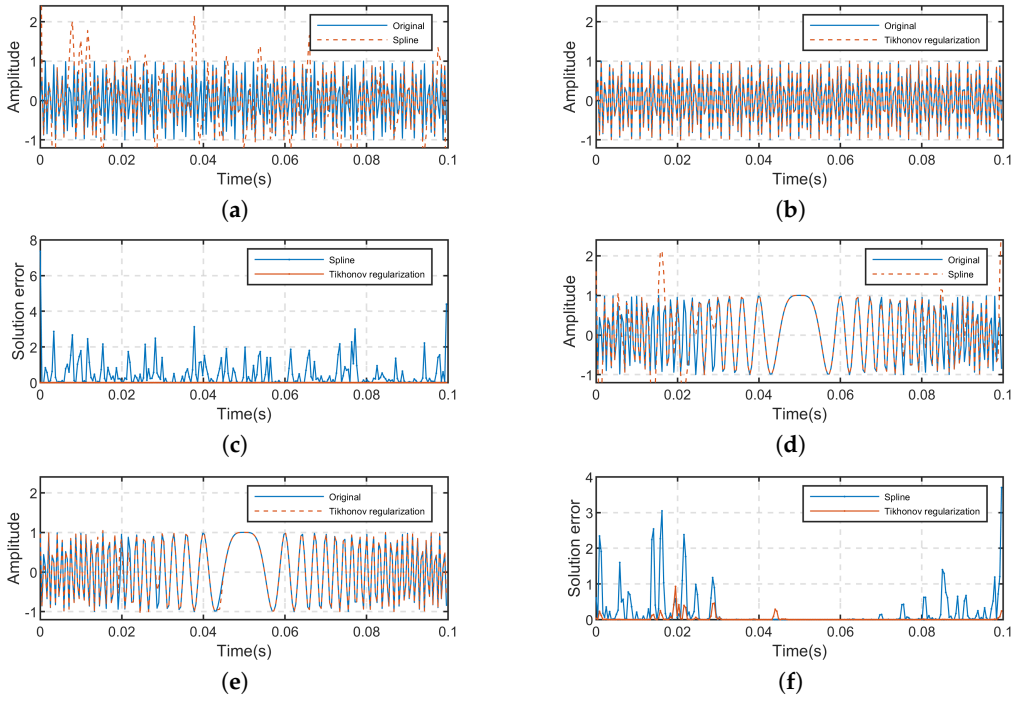


Figure 4. Reconstruction result of Spline interpolation for (**a**) $s_1(t_i^{(1)})$ and (**b**) $s_2(t_i^{(2)})$. Reconstruction result of Tikhonov regularization for (**c**) $s_1(t_i^{(1)})$ and (**d**) $s_2(t_i^{(2)})$. Comparison between the solution error of Spline interpolation and Tikhonov regularization for (**e**) $s_1(t_i^{(1)})$ and (**f**) $s_2(t_i^{(2)})$.

In SAR signal processing, the azimuth echoes located in the same range direction can be approximated as LFM signals under certain conditions. Similar to the processing of SAR azimuth echoes, we multiply the reconstructed results of $s_2(t_i^{(2)})$ obtained using the two methods by a phase function $\exp(j\pi(m\Delta f)^2/K)$ in the frequency domain and perform the IFFT operation, where K is the chirp rate of $s_2(t)$. Figure 5 shows the corresponding results and compares them with the pulse compression results of the original uniformly sampled signals. The results indicate that both cubic spline interpolation and the Tikhonov regularization method can correctly focus at $t = 0.05$ s after pulse compression. However, the result obtained using cubic spline interpolation exhibits higher sidelobes, while the Tikhonov regularization method is closer to the pulse compression result of original uniformly sampled signal. This also demonstrates the potential application of the proposed method in THz SAR azimuth non-uniform sampling problems. Further detailed discussions on this issue will be conducted in Section 4.

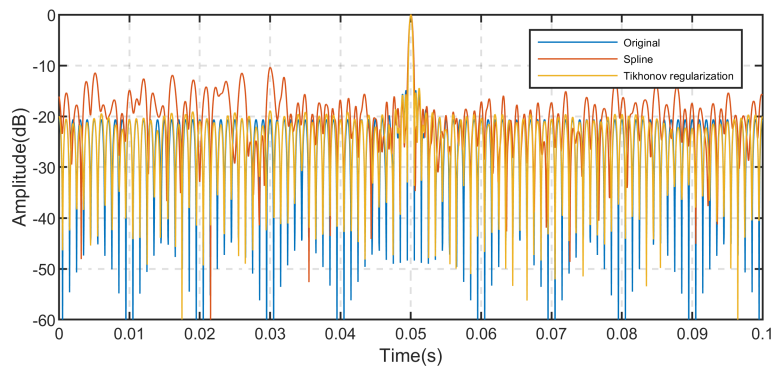


Figure 5. Comparison of pulse compression results between reconstructed signal from $s_2(t_i^{(2)})$ and original uniformly sampled signal.

4. The Application of Tikhonov Regularization in THz SAR

4.1. Wavenumber Spectrum Reconstruction Model of THz SAR Azimuth Non-Uniform Sampling Signals

Assuming that the radar platform operates in the stripmap mode with a side-looking configuration, where the platform's motion trajectory is parallel to the x-axis of the coordinate system, the radar center frequency is f_c, and the antenna beamwidth is θ_{bw}. In the fast-time domain, the number of samples for each azimuthal sampling point is N_k. Figure 6 shows the imaging geometry under non-uniform sampling conditions in the azimuth direction for the radar platform. Due to the deviation of sampling positions from the ideal uniformly sampled positions, the received echo data exhibits certain deviations. Let $x_1, x_2, x_3, \cdots\cdots x_{N_m}$ denote the non-uniform sampling positions in thr azimuth direction of the radar platform, which can be obtained through accurate inertial navigation systems or by using the raw data of SAR echo signals received by the radar platform. The position coordinates of point target B are denoted as $[x_B, y_B, 0]$, and the closest slant range AB from the radar track to point target B is denoted as R_B. The slant range from the i-th sampling position x_i to point target B is denoted as $R(x_i)$. It can be expressed as

$$R(x_i) = \sqrt{(x_i - x_B)^2 + R_B^2} \tag{19}$$

The SAR signal processing is based on the "stop and go" assumption. Under the condition that this assumption holds, the received SAR echo data can be considered as identical regardless of the platform's velocity, as long as the positions of the azimuth sampling points are fixed. Therefore, when processing the echo data in wavenumber domain, there is no need to consider the specific velocity of the radar platform [30].

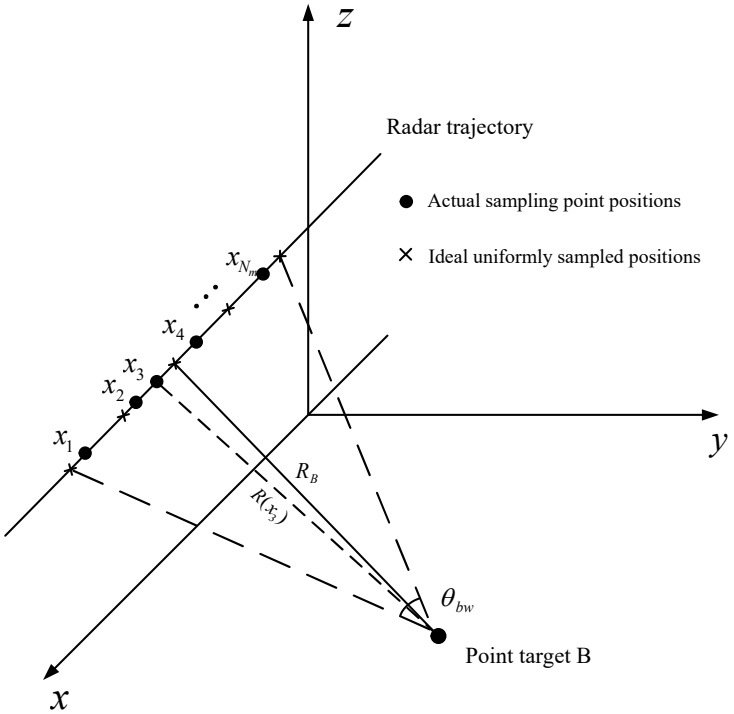


Figure 6. Azimuth non-uniform sampling imaging geometry of THz SAR.

In the case of SAR azimuth non-uniform sampling, the processing of SAR echo data in Doppler domain becomes more complicated due to uneven platform velocity. Therefore, we adopt a more convenient wavenumber domain processing method. Taking the commonly used LFM signal as an example, assuming the frequency modulation rate of radar transmission signal is K_r and the duration is T_p, neglecting the range and azimuth

envelopes of echo data and considering only the phase term, the point target model of the demodulated SAR echo signal can be expressed as

$$s_0(x, t_k) = \exp\{-j4\pi f_c R(x)/c\} \exp\{j\pi K_r (t_k - 2R(x)/c)^2\} \tag{20}$$

where c is the speed of light, x is the azimuth position, $R(x)$ represents the distance from x to point target B, and t_k represents the fast time in range direction. The ranges of t_k and x are

$$t_k \in \left[2R(x)/c - \frac{T_p}{2}, 2R(x)/c + \frac{T_p}{2}\right] \tag{21}$$

$$x \in \left[-\frac{\theta_{bw}}{2} \leq \arctan(\frac{|x - x_B|}{R_B}) \leq \frac{\theta_{bw}}{2}\right] \tag{22}$$

The range Fourier transform result can be obtained as

$$S_1(x, f_k) = \exp\{-j\frac{4\pi(f_c + f_k)R(x)}{c}\} \exp\{-j\frac{\pi f_k^2}{K_r}\} \tag{23}$$

where $f_k \in \left[-K_r T_p/2, K_r T_p/2\right]$, combining Equations (19) and (23), the azimuth Fourier transform is obtained as

$$S_2(K_x, f_k) = \exp\{-j2\pi\sqrt{\frac{4(f_c + f_k)^2}{c^2} - K_x^2} - j2\pi K_x x_B\} \exp\{-j\frac{\pi f_k^2}{K_r}\} \tag{24}$$

The relationship between the azimuth wavenumber spectrum K_x and x is given by

$$K_x = \frac{2(f_c + f_k)}{c}\left[\frac{(x_B - x)}{\sqrt{R_B^2 + (x_B - x)^2}}\right] \tag{25}$$

Let

$$\sin\theta = \frac{(x_B - x)}{\sqrt{R_B^2 + (x_B - x)^2}} \tag{26}$$

Based on the geometric relationship shown in Figure 6, θ represents the angle between the line connecting the phase center of antenna to the point target and the closest slant range AB. The relationship between θ and θ_{bw} can be expressed as

$$-\frac{\theta_{bw}}{2} < \theta < \frac{\theta_{bw}}{2} \tag{27}$$

According to Equation (25), the range of K_x can be represented as

$$-\frac{2(f_c + f_k)}{c}\sin\frac{\theta_{bw}}{2} \leq K_x \leq \frac{2(f_c + f_k)}{c}\sin\frac{\theta_{bw}}{2} \tag{28}$$

Due to the fact that f_k is within a certain frequency band, the wavenumber spectrum of the SAR azimuthal sampling signal is band-limited. Its maximum value is related to the center frequency, radar bandwidth, and antenna beamwidth. Even with the presence of azimuthal envelope functions and potential effects caused by signal truncation processing, the SAR azimuthal sampling signal can still be considered approximately band-limited.

For a given f_k, the azimuth non-uniformly sampled signal can be represented as an N_m-dimensional vector s_{f_k}, where

$$s_{f_k}(i) = S_1(x_i, f_k) \quad i = 1, 2, \cdots, N_m \tag{29}$$

Taking azimuth wavenumber spectrum interval $\Delta k < 1/(x_{N_m} - x_1)$, with

$$K_{\max} = a\frac{2(f_c + f_k)}{c}\sin\frac{\theta_{bw}}{2} \tag{30}$$

where α is the oversampling factor and $M = \lfloor K_{\max}/\Delta k \rfloor$, the wavenumber spectrum of SAR echo signal at f_k is represented as a $(2M+1)$-dimensional vector S_{f_k}, where

$$S_{f_k}(m + M + 1) = S_2(m\Delta k, f_k) \quad m = -M, -M+1, \cdots, M \tag{31}$$

The established SAR azimuthal non-uniform sampling wavenumber spectrum reconstruction model is

$$s_{f_k} = AS_{f_k} + \tilde{n}_{f_k} \tag{32}$$

where $A(i,m) = e^{j2\pi m\Delta k(x_i - x_1)}$ is a linear operator matrix of dimensions $N_m \times 2M+1$, and $\tilde{n}_{f_k}$ is the error term at range-domain frequency f_k.

4.2. Imaging Algorithm Based on Tikhonov Regularization

By using the proposed method in this paper, the azimuthal wavenumber spectrum of the SAR echo signal can be reconstructed from Equation (32). The received echo signal is an $N_m \times N_k$-dimensional data matrix. This means that we need to solve N_k linear equation systems with the same coefficient matrix A. Under the condition of SVD of A, the solution process is relatively simple and the computational complexity is mainly concentrated on the SVD of A. Additionally, for two-dimensional SAR echo data collected in the same time period, the noise level of the received signal is the same. Therefore, in the process of solving N_k linear equation systems, only one regularization parameter needs to be selected. For this purpose, we calculate the weighted average value s_f of these N_k linear equation systems, which is obtained by setting

$$s_f = \frac{1}{N_k}\sum_{k=1}^{N_k} s_{f_k} \tag{33}$$

By applying L-curve criterion, we solve for the regularization parameter of the linear equation system corresponding to s_f, which represents the regularization parameter selected for N_k linear equation systems.The proposed algorithm offers an effective solution for the reconstruction of non-uniformly sampled signals. It exhibits superior efficiency compared to interpolation-based [31], iterative [32] when handling two-dimensional non-uniformly sampled data, such as in SAR applications.

Based on the above analysis, we can combine the proposed algorithm with a Range-Doppler Algorithm (RDA) to process SAR echo data with azimuth non-uniform sampling. The corresponding algorithm flowchart is shown in Figure 7, which will be used for the simulation and imaging experiments of THz SAR in Section 5. Compared to the conventional RDA, the algorithm shown in Figure 7 transforms the processing of azimuth echo data into a wavenumber domain and replaces azimuth FFT operation with the algorithm proposed in this paper. Therefore, it can also be combined with the Range Migration Algorithm (RMA) to process SAR azimuth non-uniform sampling data, making it applicable to any imaging geometry.

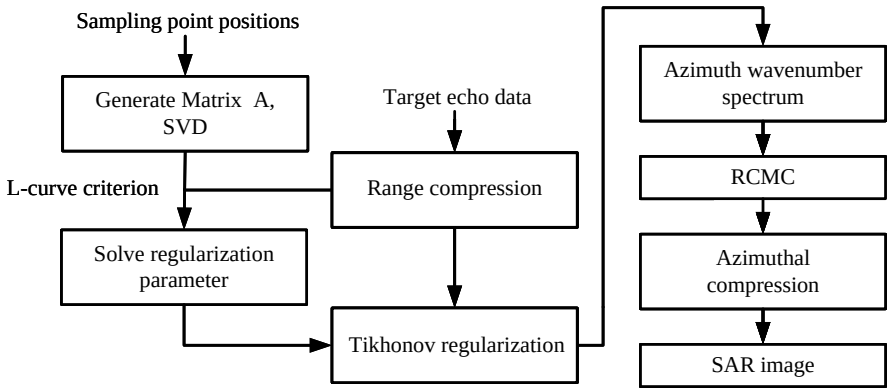


Figure 7. Flow chart of SAR imaging algorithm combining Tikhonov regularization and RDA.

5. Simulation and Experimental Results

5.1. Point Target Simulation

We conducted point target simulation for non-uniform sampling in THz SAR based on the imaging geometry shown in Figure 7. The radar parameters used are consistent with the 300 GHz stepped frequency radar system employed in the experiment, as shown in Table 1. Simulating the point target B in Figure 7, we assume that the azimuth position of B is $x_B = 4$ m and $R_B = 4$ m. The main simulation parameters are provided in Table 2.

Table 1. 300 GHz radar experimental parameters.

Parameters	Value
Frequency step size	18 MHz
Total radar bandwidth	28.8 GHz
Azimuth beamwidth	6.5°
Antenna aperture	1 cm
Transmitting power	0.5 mW

Table 2. Main simulation parameters for non-uniform sampling of point target B.

Parameters	Value
Number of Frequency steps N_k	1601
Radar center frequency f_c	300 GHz
Slant range of scene center R_c	4.167 m
Azimuth beam width θ_{bw}	6.5°
Squint angle θ_0	0°
Range resolution ρ_k	0.0052 m
Azimuth oversampling factor a	1.2
Azimuth wavenumber bandwidth $K_{\max}$	136.158 m^{-1}
Azimuth wavenumber spectral interval Δk	2.2013 m^{-1}
Number of Azimuth wavenumber spectrum $2M + 1$	125

According to the antenna beamwidth, the radar is able to effectively receive the echo data of point target B within the azimuth position range of [3.7729 m, 4.2271 m]. We conducted a simulation by randomly sampling within this range, generating echo data corresponding to the positions obtained through random sampling. We selected three sets of non-uniformly sampled echo data. The value of N_m for these three sets are 150, 200, and 250, respectively, approximately 1.2, 1.6, and 2 times the number of the azimuth wavenumber spectrum to be estimated. Figure 8 shows the sampling point positions for these three sets of echo data. The vertical axis represents the non-uniformly sampled positions in azimuth, and the horizontal axis represents the index i. A noticeable trend is that with a smaller value of N_m, the interval between these points becomes relatively larger, leading to a more uneven distribution of the obtained echo data.

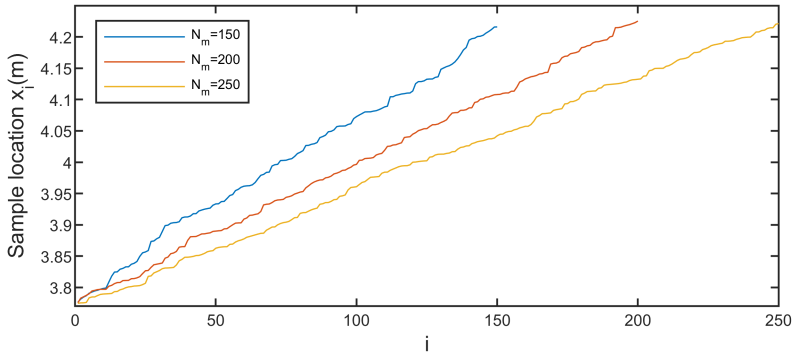


Figure 8. Non-uniform sampling position distribution of three groups of echo data.

We compared the proposed algorithm (TR-RDA) with RDA, the Azimuth Resampling Algorithm (AR-RDA) based on spline interpolation and BPA. Figure 9 shows the imaging results for the three sets of echo data. For the convenience of comparison, the results were normalized and displayed in logarithmic form, with the image range set to be above −30 dB. When RDA is directly applied to the azimuth non-uniformly sampled echo data, the imaging results showed severe defocusing. The focusing effect of point targets obtained by AR-RDA deteriorates as the value of N_m decreases due to the influence of spectral aliasing effects, while the TR-RDA and BPA algorithms exhibit relatively minor variations with changes in N_m. Moreover, from the imaging results, it is evident that the TR-RDA algorithm yields superior focusing effects compared to the results obtained by AR-RDA and BPA.

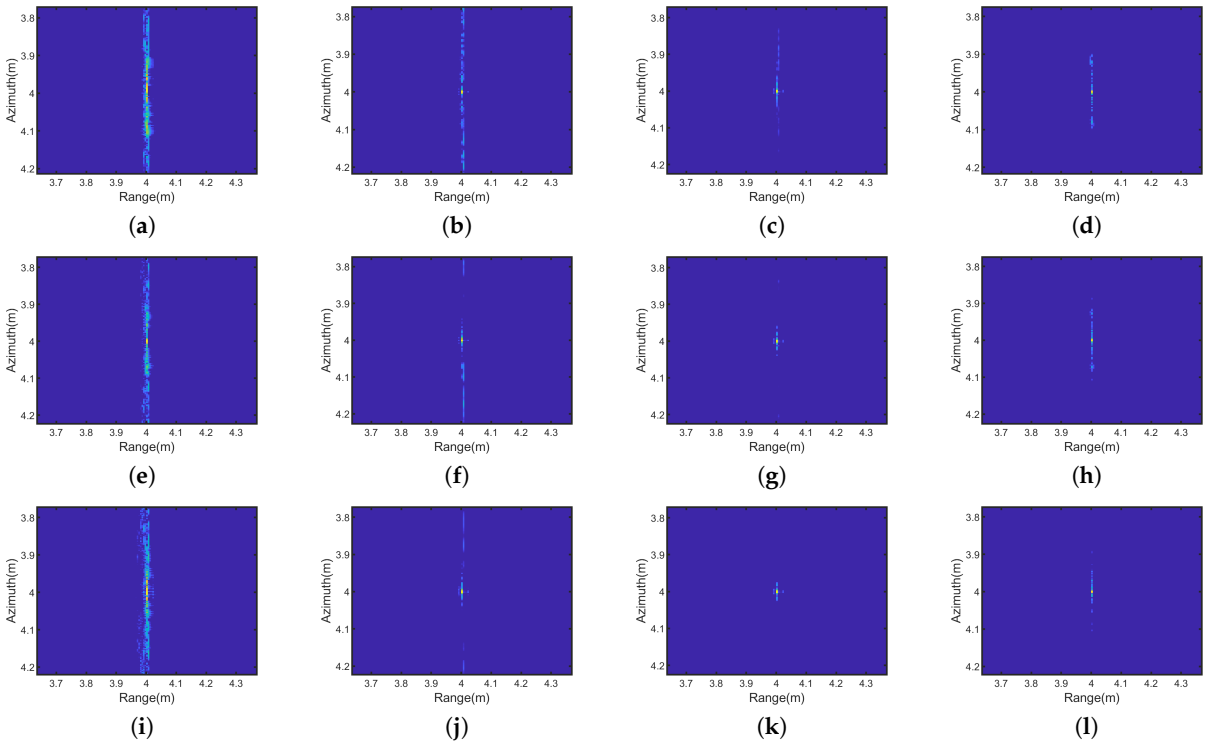


Figure 9. Imaging results of (**a**) RDA, (**b**) AR-RDA, (**c**) TR-RDA, and (**d**) BPA when $N_m = 150$. Imaging results of (**e**) RDA, (**f**) AR-RDA, (**g**) TR-RDA, and (**h**) BPA when $N_m = 150$. Imaging results of (**i**) RDA, (**j**) AR-RDA, (**k**) TR-RDA, and (**l**) BPA when $N_m = 150$.

Figure 10 shows the azimuth impulse response function (IRF) obtained from the imaging results. Corresponding characteristic parameters for the point target are presented in Table 3. The integration sidelobe ratio (ISLR) obtained by the three algorithms is consistent with the

imaging results in Figure 9: the smaller the ISLR, the better the focusing effect of point target *B*. For peak sidelobe ratio (PSLR) and impulse response width (IRW), BPA outperforms the other two algorithms, and the results obtained by AR-RDA are the poorest. Table 4 shows the time cost of the three algorithms at different N_m, which was measured on an Intel® Core™ i5-13500H CPU with a main frequency of 2.6 GHz (Intel Corporation, Santa Clara, CA, USA). It can be observed that as N_m increases, the time cost of BPA increases at a noticeably faster rate compared to the other two algorithms. This indicates that BPA requires higher computational resources. According to the simulation results, the following conclusions can be inferred: The algorithm proposed in this paper outperforms azimuth resampling in terms of accuracy. Additionally, it achieves comparable or even superior imaging effects compared to BPA, all while requiring less computational complexity.

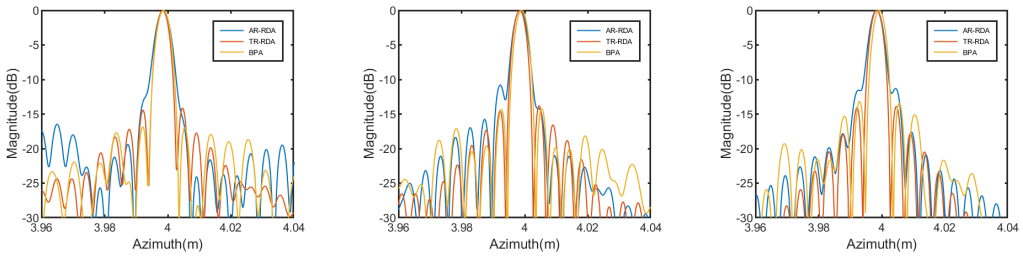


Figure 10. Pulse response function of the three algorithms to point target *B* when (**a**) $N_m = 150$, (**b**) $N_m = 200$, (**c**) $N_m = 250$.

Table 3. Azimuth pulse response characteristics of point target *B*.

N_m	Algorithm	PSLR (dB)	ISLR (dB)	IRW (m)
150	AR-RDA	−16.45	−6.2484	0.0046
	TR-RDA	−14.15	−8.8789	0.0040
	BPA	−16.83	−6.9386	0.0041
200	AR-RDA	−10.77	−7.9966	0.0043
	TR-RDA	−13.76	−9.7141	0.0040
	BPA	−14.21	−7.0163	0.0038
250	AR-RDA	−11.29	−8.5601	0.0043
	TR-RDA	−13.87	−10.6622	0.0040
	BPA	−13.16	−7.5317	0.0039

Table 4. The time cost (seconds) of the three algorithms at different N_m.

N_m	AR-RDA	TR-RDA	BPA
150	1.0955	1.2971	1.6504
200	1.1043	1.3364	2.9573
250	1.1518	1.3379	4.7433
500	1.1968	1.6514	16.3716

5.2. Experiment Results

In order to verify the effectiveness of TR-RDA in actual received signals with noise, we conducted non-uniform sampling imaging experiments using a 0.3 THz stepped-frequency radar system. The radar system parameters are presented in Table 1, with an azimuth beamwidth of 6.5 degrees and a detectable range of 0–8.333 m. The range and azimuth resolutions can reach 5 mm.

The radar operated in stripmap mode, and the raw echo data obtained by the radar exhibited uniformity in the azimuth direction. Suppose there are N uniformly sampled points in the azimuth direction. To perform non-uniform sampling imaging experiments, we selected N_m (where $N_m < N$) sampled points with non-uniform spacing from the original uniformly sampled echo data.

A total of three sets of raw data were selected for the experiments. The first and second sets correspond to the echo data obtained by imaging the letter A and an airplane model indoors, respectively, using the radar mounted on a small cart. Figure 11 shows the radar system mounted on the small cart. In the bottom left corner of Figure 11, there is a measuring wheel with a diameter of 14.8 cm. By rotating the measuring wheel a fixed distance, the radar is triggered to emit a signal, ensuring uniform sampling in the azimuth direction. The distance interval for uniform sampling is 0.646 mm. Figures 12a and 13a shows the optical images of the letter A and the airplane model. The minimum slant range from the center of letter A and airplane model to the radar sensor is approximately 1.5 m. The pixel sizes of the first and second sets of raw echo data are 1927×1601 and 1100×1601, respectively. The third set echo data was obtained by imaging a pedestrian crosswalk scene outdoors, as shown in Figure 14, using the radar mounted on the top of a car. The radar system has a coverage range of approximately 5 m to 7 m. To maintain uniform sampling in the azimuth direction, a measuring wheel with a diameter of 72 cm was mounted on the car too, providing a sampling interval of 1.8 mm. The pixel size of the raw echo data obtained is 4313×1601.

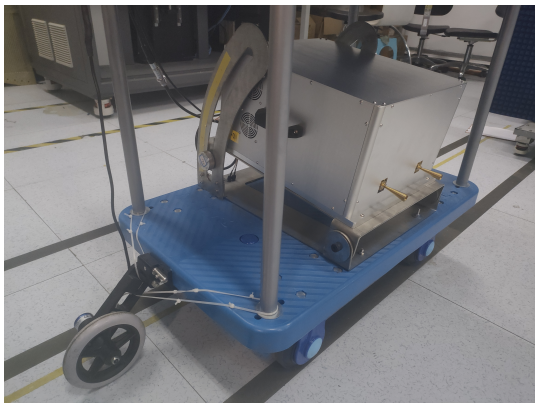


Figure 11. Experimental setup diagram loaded on a small cart.

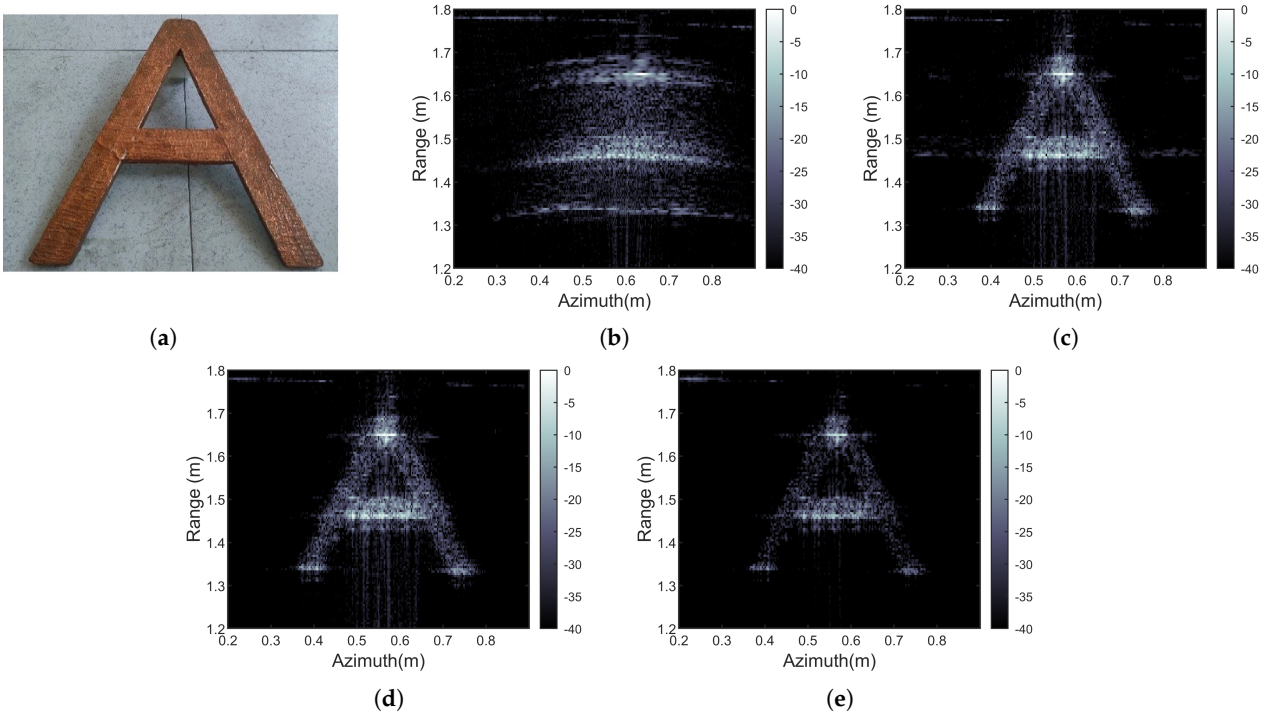


Figure 12. (**a**) Letter A optical image; (**b**) RDA; (**c**) AR-RDA; (**d**) TR-RDA; (**e**) BPA.

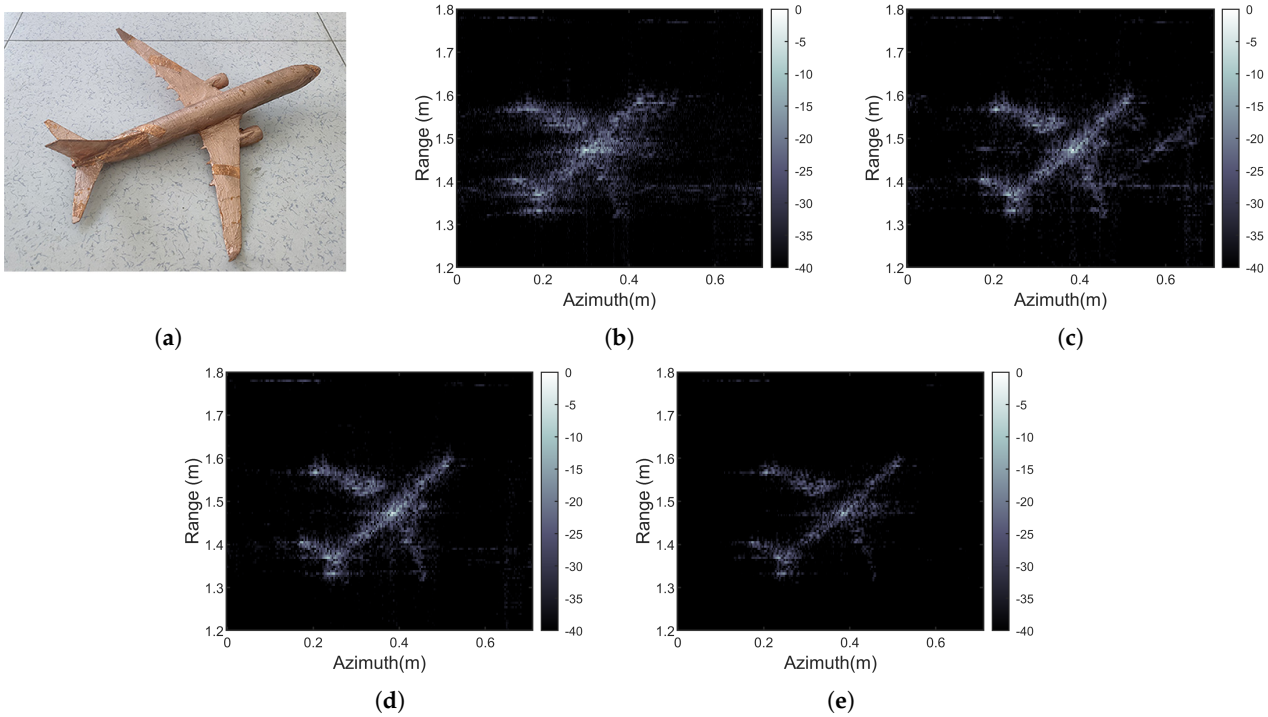


Figure 13. (**a**) airplane model optical image; (**b**) RDA; (**c**) AR-RDA; (**d**) TR-RDA; (**e**) BPA.



Figure 14. Pedestrian crossing scene optical image.

For these three sets of raw echo data, we selected N_m values of 1156, 551, and 1922, respectively. Figure 15 shows the interval size between the non-uniformly sampled points for these three sets of data. The y-axis represents the interval between adjacent non-uniformly sampled positions, denoted as $x_i - x_{i-1}$ $(2 \leq i \leq N_m)$, and the x-axis represents the index i. Since these three sets of echo data originate from the same THz radar system, the larger the non-uniform sampling interval, the more uneven the obtained non-uniform sampling data. The selected first set of data exhibits a relatively regular interval between the positions of the sampled points, and it has the smallest non-uniform sampling interval. The second and third sets of data were obtained using random sampling, but the third set is based on sparser raw echo data, resulting in larger non-uniform sampling intervals compared to the other two sets of data.

For the proposed algorithm, the wavenumber spectrum interval $\Delta k = 1/(x_{N_m} - x_1) \times N/(N-1)$, and the model parameters are calculated as shown in Table 5. Figures 12, 13 and 16 show the imaging results for these three sets of non-uniformly sampled data. In Figure 16, the regions where substantial differences exist

among the three algorithms are marked by red boxes. We evaluate the imaging quality using image entropy, and the results are presented in Table 6. The experimental results indicate that, compared to the other three non-uniform sampling image reconstruction algorithms, the image focusing effect obtained by using the traditional RDA algorithm to process the non-uniform sampling echo data is poor. As shown in Figure 12c–e, all three algorithms yield satisfactory imaging results for the first set of data with denser sampling points. However, for the other two sets of data with larger non-uniform sampling intervals, AR-RDA does not yield satisfactory results, as evident from the noticeable blurring in Figures 13c and 16a. Furthermore, within the red box region on the right side of Figure 16c, the imaging results of BPA exhibit certain geometry distortions as a result of the non-uniformity of the sampling positions.

Table 5. Parameters of non-uniform sampling signal model.

	a	Δk $(\mathbf{m}^{-1})$	$K_{\max}$ $(\mathbf{m}^{-1})$	M
First set of data	1.6	0.8037	181.544	226
Second set of data	1.2	1.4052	136.158	97
Third set of data	1.1	0.0921	124.8115	1356

It can be seen that the experimental results are consistent with the simulation results, both of which validate the effectiveness of the proposed algorithm in this paper. Compared to the other two algorithms, the proposed algorithm possesses a unique advantage of simultaneously balancing accuracy and computational complexity.

Table 6. Image entropy of imaging results from three algorithms.

Algorithm	AR-RDA	TR-RDA	BPA
First set of data	2.1339	2.0129	1.8183
Second set of data	2.3617	2.1484	1.7142
Third set of data	12.8971	12.8715	12.8710

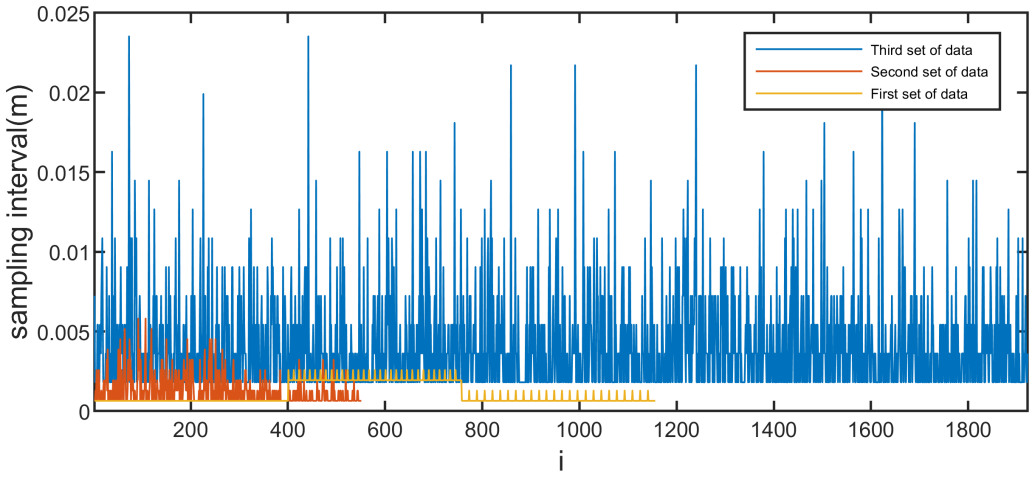


Figure 15. Interval size between non-uniform sampling point positions of two sets of data.

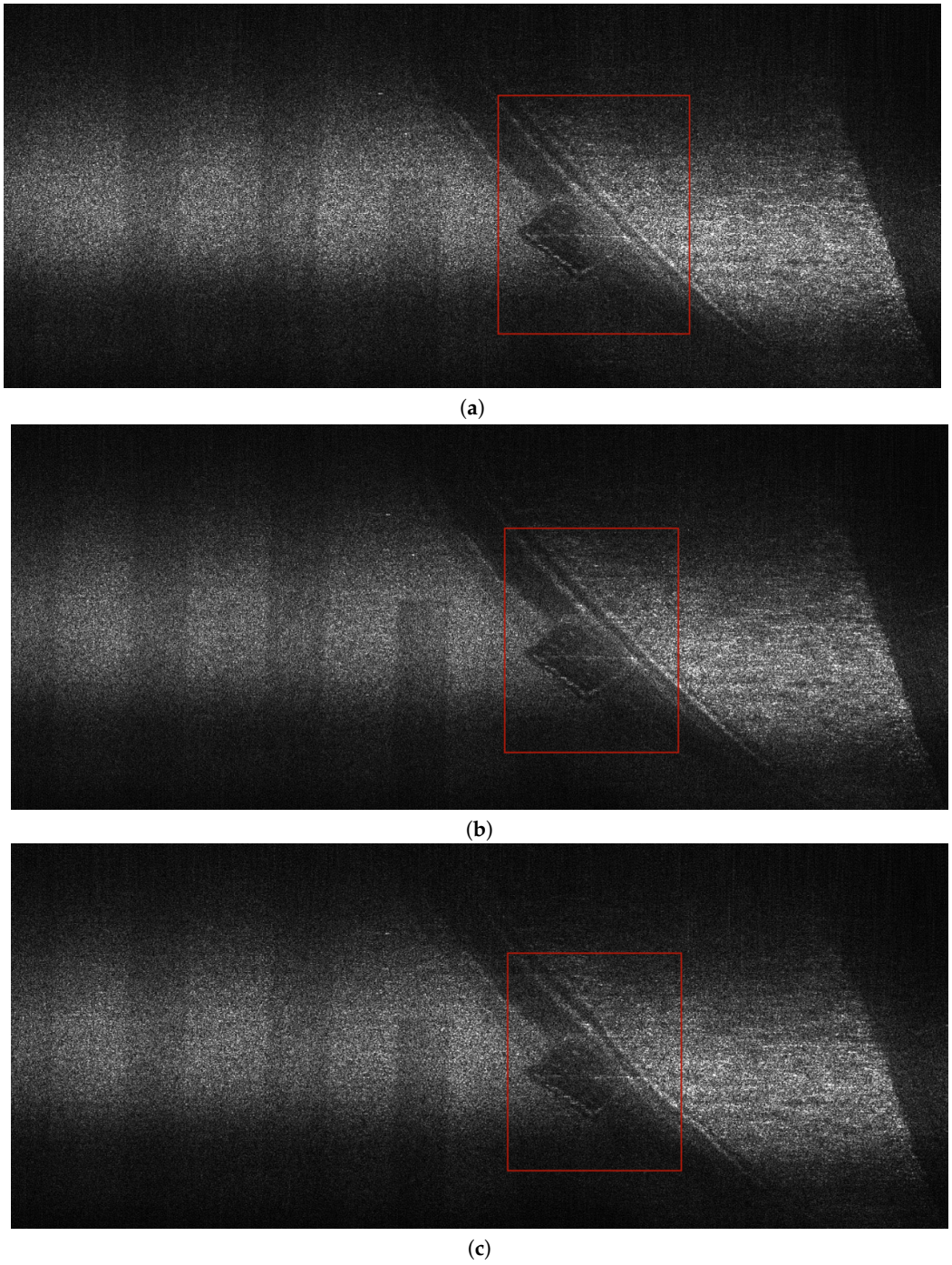


Figure 16. (**a**) AR-RDA; (**b**) TR-RDA; (**c**) BPA.

6. Conclusions

For the problem of THz SAR with azimuth non-uniform sampling, this paper proposes a wavenumber spectrum reconstruction algorithm based on Tikhonov regularization. The proposed algorithm can be combined with conventional frequency domain imaging algorithms such as RDA, CSA, and RMA, and is applicable to different imaging distances, including vehicle-mounted and airborne scenarios. In this paper, the spectral reconstruction model for non-uniformly sampled signals is established. The principle of spectral reconstruction is derived using a Fourier series, demonstrating that the estimation accuracy of the spectrum depends on the high-frequency components beyond signal bandwidth and noise for finite-length approximately band-limited signals. The azimuth echo data are processed in the wavenumber domain without considering the complex factors of

platform motion speed. Simulation and experimental results demonstrate the effectiveness of the proposed algorithm. Compared to azimuthal resampling algorithms, the proposed algorithm reduces the impact of spectral aliasing and achieves better imaging results. Compared to the BPA, it also has higher computational efficiency, making it more suitable for compensating the large azimuth motion errors in THz SAR. Additionally, the simulation analysis results not only demonstrate the good signal reconstruction performance of the proposed algorithm in THz SAR imaging but also indicate its wide application prospects in the field of signal recovery.

Author Contributions: Conceptualization, G.Z. and C.L.; methodology, G.Z.; software,W.Z.; validation, G.Z; formal analysis, G.Z. andW.Z.; investigation, G.Z.; resources, C.L.; data curation, J.H.; writing—original draft preparation, G.Z.; writing—review and editing, G.Z. and C.L.; visualization, W.Z.; supervision, X.L.; project administration, G.F.; funding acquisition, C.L. and S.Z. All authors have read and agreed to the published version of the manuscript. All authors have read and agreed to the published version of the manuscript.

Funding: This research was funded by the Beijing Municipal Natural Science Foundation under Grant L223007; the Key-Area Research and Development Program of Guangdong Province under Grant 2020B0101110001; the National Natural Science Foundation of China under Grant 61988102 and 61731020; the National Key Research and Development Program of China under Grant 2017YFA0701004; the Project of Equipment Pre-Research under Grant WJ2019G00019; and the Key Program of Scientific and Technological Innovation from Chinese Academy of Sciences under Grant KGFZD-135-18-029.

Data Availability Statement: Not applicable.

Conflicts of Interest: The authors declare no conflict of interest.

Appendix A

In this appendix, we provide the derivation process of (17). Based on the singular value decomposition of A, we can get

$$A^* u_j = \sigma_j v_j, \quad j = 1, \cdots, 2M+1. \tag{A1}$$

Combining (10), the solution error between $S_{\tilde{n}}^{\alpha}$ and S can be represented as

$$\begin{aligned} \left\| S_{\tilde{n}}^{\alpha} - S \right\| &\leq \| R_\alpha s_\delta - R_\alpha AS \| + \| R_\alpha AS - S \| \\ &\leq \| R_\alpha \| \| s_\delta - AS \| + \| R_\alpha AS - S \| \\ &\leq \| R_\alpha \| \| \tilde{n} \| + \| R_\alpha AS - S \| \end{aligned} \tag{A2}$$

where the first term on the right-hand side represents the error due to the presence of $\tilde{n}$, which is amplified by the norm of R_α. The second term represents the error caused by the approximation of the discontinuous operator A^{-1} by R_α.

According to (15), for any $0 < \sigma_j \leq \|A\|$, $\alpha > 0$, we have

$$\left| q(\alpha, \sigma_j) \right| \leq \frac{\sigma_j}{2\alpha} \tag{A3}$$

$$\left| q(\alpha, \sigma_j) - 1 \right| \leq \frac{\alpha}{2\sigma_j}. \tag{A4}$$

For $\forall s \in C^N$, we can get

$$\| R_\alpha s \|^2 = \sum_{j=1}^{2M+1} \left[q(\alpha, \sigma_j) \right]^2 \frac{1}{\sigma_j^2} \left| \langle s, u_j \rangle \right|^2 \leq \frac{1}{4\alpha^2} \sum_{j=1}^{2M+1} \left| \langle s, u_j \rangle \right|^2 \leq \frac{1}{4\alpha^2} \| s \|^2. \tag{A5}$$

This indicates that $\|R_\alpha\| \leq 1/2\alpha$. The vector v_j represents a set of orthonormal bases in the complex space C^{2M+1}. The S can be expressed as

$$S = \sum_{j=1}^{2M+1} \langle S, v_j \rangle v_j. \tag{A6}$$

Combining it with (A1), we can get

$$\begin{aligned} \|R_\alpha AS - S\|^2 &= \left\| \sum_{j=1}^{2M+1} \frac{q(\alpha, \sigma_j)}{\sigma_j} \langle AS, u_j \rangle v_j - \sum_{j=1}^{2M+1} \langle S, v_j \rangle v_j \right\|^2 \\ &= \left\| \sum_{j=1}^{2M+1} \frac{q(\alpha, \sigma_j)}{\sigma_j} \langle S, A^* u_j \rangle v_j - \sum_{j=1}^{2M+1} \langle S, v_j \rangle v_j \right\|^2 \\ &= \sum_{j=1}^{2M+1} |q(\alpha, \sigma_j) - 1|^2 |\langle S, v_j \rangle|^2 \\ &\leq \tfrac{\alpha^2}{4} \sum_{j=1}^{2M+1} \tfrac{1}{\sigma_j^2} |\langle S, v_j \rangle|^2. \end{aligned} \tag{A7}$$

Let

$$z = \sqrt{\sum_{j=1}^{2M+1} \frac{1}{\sigma_j^2} |\langle S, v_j \rangle|^2} \tag{A8}$$

then $\|R_\alpha AS - S\| \leq \frac{\alpha}{2} z$. (A2) can be simplified as

$$\left\| S_{\tilde{n}}^{\alpha} - S \right\| = \left\| \sum_{j=1}^{2M+1} \left[\frac{q(\alpha, \sigma_j)}{\sigma_j} \langle \tilde{n}, v_j \rangle + \big(q(\alpha, \sigma_j) - 1\big) \langle S, v_j \rangle \right] v_j \right\| \leq \frac{1}{2\alpha} \|\tilde{n}\| + \frac{\alpha}{2} z. \tag{A9}$$

References

1. Lee, J.; Pottier, E. *Polarimetric Radar Imaging: From Basics to Applications*; Optical Science and Engineering; CRC Press: Boca Raton, FL, USA, 2009; pp. 1–398. [CrossRef]
2. Xu, Z.; Lu, P.; Cai, Y.; Li, J.; Yang, T.; Wu, Y.; Wang, R. An Efficient Channel Imbalance Estimation Method Based on Subadditivity of Linear Normed Space of Sub-Band Spectrum for Azimuth Multichannel SAR. *Remote Sens.* **2023**, *15*, 1561. [CrossRef]
3. Shi, S.; Li, C.; Hu, J.; Zhang, X.; Fang, G. Study of Phase Error Reconstruction and Motion Compensation for Terahertz SAR with Sparsity-Promoting Parameter Estimation. *IEEE Trans. Terahertz Sci. Technol.* **2021**, *11*, 122–134. [CrossRef]
4. Kim, S.H.; Fan, R.; Dominski, F. ViSAR: A 235 GHz radar for airborne applications. In Proceedings of the 2018 IEEE Radar Conference (RadarConf18), Oklahoma City, OK, USA, 23–27 April 2018; pp. 1549–1554. [CrossRef]
5. Fang, J.; Gong, X. Predictive Iterated Kalman Filter for INS/GPS Integration and Its Application to SAR Motion Compensation. *IEEE Trans. Instrum. Meas.* **2010**, *59*, 909–915. [CrossRef]
6. Fornaro, G. Trajectory deviations in airborne SAR: Analysis and compensation. *IEEE Trans. Aerosp. Electron. Syst.* **1999**, *35*, 997–1009. [CrossRef]
7. Moreira, A.; Huang, Y. Airborne SAR processing of highly squinted data using a chirp scaling approach with integrated motion compensation. *IEEE Trans. Geosci. Remote Sens.* **1994**, *32*, 1029–1040. [CrossRef]
8. Zhou, S.; Yang, L.; Zhao, L.; Bi, G. Forward Velocity Extraction From UAV Raw SAR Data Based on Adaptive Notch Filtering. *IEEE Geosci. Remote Sens. Lett.* **2016**, *13*, 1211–1215. [CrossRef]
9. Reigber, A.; Alivizatos, E.; Potsis, A.; Moreira, A. Extended wavenumber-domain synthetic aperture radar focusing with integrated motion compensation. *IEE Proc. Radar Sonar Navig.* **2006**, *153*, 301–310. [CrossRef]
10. Meng, D.; Hu, D.; Ding, C. Precise Focusing of Airborne SAR Data with Wide Apertures Large Trajectory Deviations: A Chirp Modulated Back-Projection Approach. *IEEE Trans. Geosci. Remote Sens.* **2015**, *53*, 2510–2519. [CrossRef]
11. de Macedo, K.; Scheiber, R. Precise topography- and aperture-dependent motion compensation for airborne SAR. *IEEE Geosci. Remote Sens. Lett.* **2005**, *2*, 172–176. [CrossRef]
12. Prats, P.; Camara de Macedo, K.A.; Reigber, A.; Scheiber, R.; Mallorqui, J.J. Comparison of Topography- and Aperture-Dependent Motion Compensation Algorithms for Airborne SAR. *IEEE Geosci. Remote Sens. Lett.* **2007**, *4*, 349–353. [CrossRef]

13. Ding, Z.; Liu, L.; Zeng, T.; Yang, W.; Long, T. Improved Motion Compensation Approach for Squint Airborne SAR. *IEEE Trans. Geosci. Remote Sens.* **2013**, *51*, 4378–4387. [CrossRef]
14. Zeng, L.; Liang, Y.; Xing, M.; Huai, Y.; Li, Z. A Novel Motion Compensation Approach for Airborne Spotlight SAR of High-Resolution and High-Squint Mode. *IEEE Geosci. Remote Sens. Lett.* **2016**, *13*, 429–433. [CrossRef]
15. Yang, M.; Zhu, D. Efficient Space-Variant Motion Compensation Approach for Ultra-High-Resolution SAR Based on Subswath Processing. *IEEE J. Sel. Top. Appl. Earth Obs. Remote Sens.* **2018**, *11*, 2090–2103. [CrossRef]
16. Blacknell, D.; Freeman, A.; Quegan, S.; Ward, I.; Finley, I.; Oliver, C.; White, R.; Wood, J. Geometric accuracy in airborne SAR images. *IEEE Trans. Aerosp. Electron. Syst.* **1989**, *25*, 241–258. [CrossRef]
17. Xing, M.; Jiang, X.; Wu, R.; Zhou, F.; Bao, Z. Motion Compensation for UAV SAR Based on Raw Radar Data. *IEEE Trans. Geosci. Remote Sens.* **2009**, *47*, 2870–2883. [CrossRef]
18. Nashed, M.Z. The Theory of Tikhonov Regularization for Fredholm Equations of the First Kind (C. W. Groetsch). *SIAM Rev.* **1986**, *28*, 116–118. [CrossRef]
19. Gao, Y.; Xing, M.; Guo, L.; Zhang, Z. Extraction of Anisotropic Characteristics of Scattering Centers and Feature Enhancement in Wide-Angle SAR Imagery Based on the Iterative Re-Weighted Tikhonov Regularization. *Remote Sens.* **2018**, *10*, 2066. [CrossRef]
20. Calvetti, D.; Morigi, S.; Reichel, L.; Sgallari, F. Tikhonov regularization and the L-curve for large discrete ill-posed problems. *J. Comput. Appl. Math.* **2000**, *123*, 423–446. [CrossRef]
21. Feichtinger, H.G.; Gröchenig, K.; Strohmer, T. Efficient numerical methods in non-uniform sampling theory. *Numer. Math.* **1995**, *69*, 423–440. [CrossRef]
22. Cooley, J.W.; Tukey, J.W. An Algorithm for the Machine Calculation of Complex Fourier Series. *Math. Comput.* **1965**, *19*, 297–301. [CrossRef]
23. Papoulis, A. A new algorithm in spectral analysis and band-limited extrapolation. *IEEE Trans. Circuits Syst.* **1975**, *22*, 735–742. [CrossRef]
24. Jerri, A. The Shannon sampling theorem—Its various extensions and applications: A tutorial review. *Proc. IEEE* **1977**, *65*, 1565–1596. [CrossRef]
25. Hansen, P.C. The Discrete Picard Condition for Discrete Ill-Posed Problems. *BIT Numer. Math.* **1990**, *30*, 658–672. [CrossRef]
26. Hansen, P.C. Perturbation bounds for discrete Tikhonov regularisation. *Inverse Probl.* **1989**, *5*, L41. [CrossRef]
27. Tikhonov, A.N. Solution of incorrectly formulated problems and the regularization method. *Sov. Math. Dokl.* **1963**, *4*, 1035–1038.
28. Hansen, P.C.; O'Leary, D.P. The Use of the L-Curve in the Regularization of Discrete Ill-Posed Problems. *SIAM J. Sci. Comput.* **1993**, *14*, 1487–1503. [CrossRef]
29. Varah, J.M. Pitfalls in the Numerical Solution of Linear Ill-Posed Problems. *SIAM J. Sci. Stat. Comput.* **1983**, *4*, 164–176. [CrossRef]
30. Bi, H.; Wang, J.; Bi, G. Wavenumber Domain Algorithm-Based FMCW SAR Sparse Imaging. *IEEE Trans. Geosci. Remote Sens.* **2019**, *57*, 7466–7475. [CrossRef]
31. Maymon, S.; Oppenheim, A.V. Sinc Interpolation of Nonuniform Samples. *IEEE Trans. Signal Process.* **2011**, *59*, 4745–4758. [CrossRef]
32. Marvasti, F.; Analoui, M.; Gamshadzahi, M. Recovery of signals from nonuniform samples using iterative methods. *IEEE Trans. Signal Process.* **1991**, *39*, 872–878. [CrossRef]

Disclaimer/Publisher's Note: The statements, opinions and data contained in all publications are solely those of the individual author(s) and contributor(s) and not of MDPI and/or the editor(s). MDPI and/or the editor(s) disclaim responsibility for any injury to people or property resulting from any ideas, methods, instructions or products referred to in the content.